Volume 11 | Number 8 | August 2018 | Pages 1913–2280

Energy & Environmental Science

rsc.li/ees

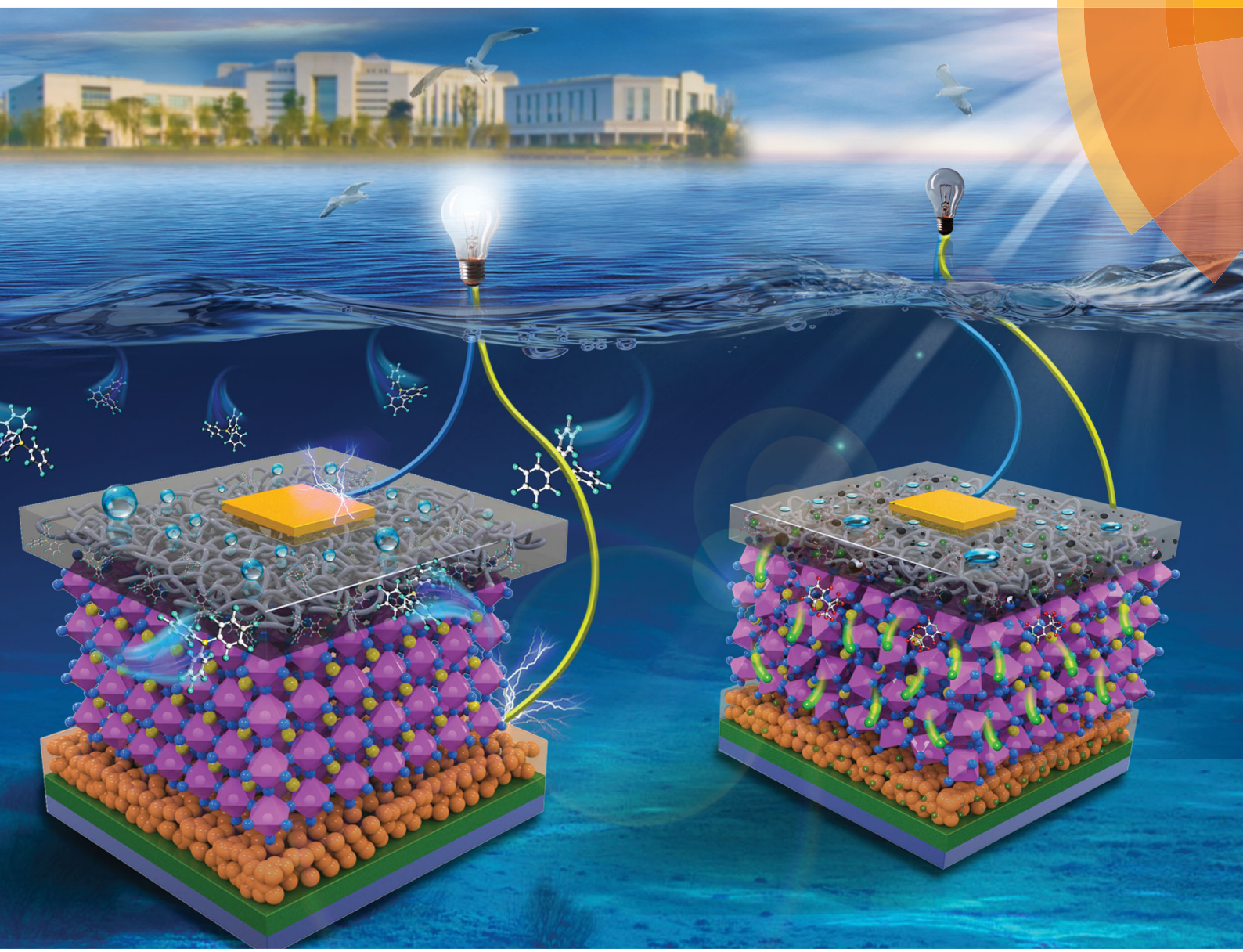

ISSN 1754-5706

ROYAL SOCIETY OF CHEMISTRY

PAPER

Chunyang Jia *et al.*

Toward high-efficiency, hysteresis-less, stable perovskite solar cells: unusual doping of a hole-transporting material using a fluorine-containing hydrophobic Lewis acid

Energy & Environmental Science

PAPER

View Article Online
View Journal | View Issue

Cite this: *Energy Environ. Sci.*, 2018, **11**, 2035

Toward high-efficiency, hysteresis-less, stable perovskite solar cells: unusual doping of a hole-transporting material using a fluorine-containing hydrophobic Lewis acid†

Junsheng Luo,[a] Jianxing Xia,[a] Hua Yang,[b] Lingling Chen,[c] Zhongquan Wan,[a] Fei Han,[a] Haseeb Ashraf Malik,[a] Xuhui Zhu [c] and Chunyang Jia *[a]

Received 4th January 2018,
Accepted 4th April 2018

DOI: 10.1039/c8ee00036k

rsc.li/ees

Perovskite solar cells (PSCs) have demonstrated high power conversion efficiency (PCE) but inferior long-term stability and remarkable hysteresis. To date, the most efficient PSCs have a n–i–p device architecture and use Li-TFSI/*t*-BP as standard bi-dopants for the hole-transporting layer (HTL). However, such dopants not only induce deleterious effects on stability but also significantly affect the hysteresis of PSCs. Here, we demonstrate that a fluorine-containing hydrophobic Lewis acid dopant (LAD) can be employed as an effective dopant for PTAA to realize an exceptional fill factor of 0.81 and a record PCE as high as 19.01%, the highest value among the ever reported PSCs based on a novel dopant in the HTL, *versus* 17.77% for the control device with Li-TFSI/*t*-BP doped PTAA. To the best of our knowledge, this is the first case in which a PSC based on a novel dopant for the HTL shows higher efficiency than a PSC based on the state-of-the-art bi-dopants Li-TFSI/*t*-BP. Besides, the LAD-based PSC displays lower *J*–*V* hysteresis and much better long-term stability of up to 70 days under air exposure without encapsulation. We believe that this work will pave a new avenue for high-efficiency, hysteresis-less and stable PSCs exploring hydrophobic dopants as alternatives to hydrophilic Li-TFSI/*t*-BP.

Broader context

Perovskite solar cells (PSCs) are promising, cost-effective, solution processed thin film photovoltaics that already exhibit superb power conversion efficiency (PCE), but suffer from challenging hysteresis and environmental instability. So far, the discussion about hysteresis and stability has been mainly focused on additive engineering in perovskite films and the electron-transporting layer. However, investigations into the hole-transporting layer (HTL) remain relatively limited. The HTL as a charge selective layer in PSCs plays a particularly important role in achieving high efficiency as well as preventing direct contact between perovskite and moisture in the air. It is known that the bi-dopants (Li-TFSI/*t*-BP) are necessary in the HTL in order to improve the hole conductivity of the HTL as well as to obtain high efficiency in PSCs, but the bi-dopants can potentially induce device hysteresis and instability due to the deliquescent, hygroscopic and ionic nature. Here, we demonstrate that fluorine-containing hydrophobic Lewis acid LAD can be employed as an effective dopant for PTAA to replace state-of-the-art bi-dopants Li-TFSI/*t*-BP and realize a PCE value as high as 19.01%, a new record among the reported PSCs based on novel dopants for the HTL, with lower *J*–*V* hysteresis and much better long-term stability of up to 70 days under air exposure without encapsulation. This work highlights the important roles of HTL dopants on the efficiency, hysteresis and stability of PSCs and opens up a new approach for designing hydrophobic HTL dopants to further advance perovskite technology for various applications.

Introduction

Organic–inorganic halide perovskite solar cells (PSCs) have drawn enormous attention and shown breathtaking development in recent years, which are attributed to the remarkable advantages of the extraordinary perovskite materials, such as high optical absorption coefficients, tunable band gaps, outstanding charge carrier mobility and long charge diffusion length.[1–5] Benefited from careful modification of perovskites, delicate design of device configurations and in-depth understanding of interfacial interactions, the power conversion efficiency (PCE) of PSCs has been dramatically improved

[a] *State Key Laboratory of Electronic Thin Films and Integrated Devices, School of Electronic Science and Engineering, University of Electronic Science and Technology of China, Chengdu 610054, P. R. China. E-mail: cyjia@uestc.edu.cn*
[b] *Dongguan Neutron Science Center, Dongguan 523803, P. R. China*
[c] *State Key Laboratory of Luminescent Materials and Devices, Institute of Polymer Optoelectronic Materials and Devices, South China University of Technology, Guangzhou 510640, P. R. China*

† Electronic supplementary information (ESI) available. See DOI: 10.1039/c8ee00036k

from initially reported 3.81% to a certified value of 22.7%.[6–13] Meanwhile, the theoretical efficiency limit of a PSC has been estimated to be 31% taking into account the photon recycling design through a detailed balance model.[14] These render PSCs as potential candidates for next-generation thin film photovoltaics.

Despite great progress in the PCE of PSCs, some issues, such as the photocurrent density–voltage (J–V) hysteresis and long term stability, are still needed to be rationally addressed for the large-scale application.[15,16] Current works aiming to reduce the hysteresis and enhance the stability in PSCs are majorly focused on additive engineering in the electron-transporting layer (ETL)[17–21] and perovskite intrinsic layer[22–28] to balance charge transport and promote perovskite quality. However, the hysteresis and stability not only originate from the unbalanced charge transport and poor perovskite quality, but also are closely related to the hole-transporting layer (HTL) as well as corresponding dopants.[29] Unfortunately, the influence of HTL dopants on hysteresis and stability of PSCs has been largely overlooked and so far only few researchers have investigated these issues.[30–36]

Currently, bis(trifluoromethane)sulfonimide lithium salt (Li-TFSI) and 4-*tert*-butylpyridine (*t*-BP) are used as standard bi-dopants for hole-transporting materials including the state-of-the-art Spiro-OMeTAD and PTAA for highly efficient PSCs (Fig. S1, ESI†). Unfortunately, Li-TFSI and *t*-BP are detrimental to the hysteresis and stability.[29,37] On the one hand, Li-TFSI has deliquescent and hygroscopic nature, which attracts water molecules and causes quick degradation of the HTL as well as the perovskite film, diminishing the stability of the device.[38] In addition, the ion behavior of Li-TFSI also strongly affects the hysteresis of PSCs. On the other hand, *t*-BP induces instability of PSCs due to its relatively low boiling point, which is easily evaporated during device fabrication and long-term storage.[39] Meanwhile, *t*-BP gives rise to the chemical decomposition of the perovskite by forming a [PbI_2·*t*-BP] coordinated complex.[40] Alternately, iodine may react with *t*-BP to form an iodopyridinate complex.[41] Given this background, it is highly desirable to develop novel dopants for HTLs to replace the commonly used Li-TFSI/*t*-BP as soon as possible. Evidently, so far there has been no substantial report on any new HTL dopant which can challenge the performance of the state-of-the-art bi-dopants Li-TFSI/*t*-BP.

In this work, we report a TiO_2 n–i–p type PSC with an exceptional fill factor (FF) of 0.81 and efficiency of 19.01% utilizing a fluorine-containing hydrophobic Lewis acid dopant (LAD, Fig. 1) for PTAA, which represents the best efficiency among reported novel dopants for HTLs and also outperforms the state-of-the-art bi-dopants Li-TFSI/*t*-BP (17.77%) for the first time. Further, the hysteresis is clearly reduced and the stability against ambient conditions is unprecedentedly enhanced for the LAD-based PSCs.

Results and discussion

Doping mechanism

Fig. 1a depicts the mechanism of LAD doping in PTAA. The triphenylamine moiety on the PTAA provides an accessible lone-pair of electrons that can associate with the LAD and form the Lewis acid–base adduct, leading to increase the free hole density and the charge-carrier mobility.[42] The adduct formation can be directly demonstrated by the color change of the LAD doped PTAA solutions (Fig. S2 and S3, ESI†). The dopant-free PTAA solution is transparent with a slight yellow color, which turns red-brown immediately upon addition of LAD. The change in color indicates that LAD effectively p-dopes PTAA and forms the Lewis acid–base adduct PTAA-LAD. Further, this adduct-solution regains its initial color *via* addition of Lewis base (such as *t*-BP). This transformation is attributed to the removal of LAD from the PTAA and the formation of the new *t*-BP-LAD adduct. In addition, the UV-Vis absorption and electron spin resonance spectra (ESR) were further evaluated to confirm the formation of the Lewis acid–base adduct PTAA-LAD. As shown in Fig. 1b, the dopant-free PTAA shows a maximum absorption peak at 379 nm. As 5% LAD (molar ratio with respect to the repeat unit of PTAA) was added, there was a decrease in the main absorption peak center and a growth in a new absorption peak at 438 nm, which was assigned to the formation of radicals.[42] The ESR spectrum also confirms the formation of the organic radical in the doped PTAA film. As shown in Fig. 1c, the LAD-doped PTAA film reveals a strong radical signal, while no appreciable signal is observed in the dopant-free PTAA film. This illustrates the strong electron-accepting ability of LAD, resulting in electron transfer from the nitrogen atoms of PTAA to the boron atoms of LAD. Therefore, these changes in absorption and ESR are consistent with PTAA-LAD formation. Electronic structure calculations were performed at the B3LYP/6-31G* level of density functional theory.[43] Fig. S4 (ESI†) shows the representation of the optimized structure, the highest occupied molecular orbital (HOMO) and lowest unoccupied molecular orbital (LUMO) topologies for LAD, indicating that LAD has a spiral configuration, and the HOMO is clearly more localized at the benzene moieties while the LUMO is primarily localized on the whole molecule.

Hole mobility and energy levels

To investigate the hole-transporting property of PTAA with different dopants, the hole-only devices were fabricated with configurations of indium tin oxide (ITO)/(poly(3,4-ethylenedioxythiophene):polystyrene-PEDOT:PSS)/dopant-free PTAA (5% LAD and Li-TFSI/*t*-BP doped PTAA)/MoO_3/Al and were evaluated using the space charge-limited current (SCLC) method. The hole mobility value of the Li-TFSI/*t*-BP doped PTAA is 4.28×10^{-4} cm^2 V^{-1} s^{-1}, which is one order of magnitude higher than that of the dopant-free PTAA (7.47×10^{-5} cm^2 V^{-1} s^{-1}, Fig. S5, ESI†). Meanwhile, the 5% LAD doped PTAA exhibits hole mobility as high as 5.72×10^{-4} cm^2 V^{-1} s^{-1}, which is higher than Li-TFSI/*t*-BP doped PTAA. The improved hole mobility will contribute to efficient hole transport and extraction, hence increasing the overall efficiency in PSCs.

Chemical doping also plays a critical role in adjusting the energy levels of organic semiconductors, correspondingly influencing the photovoltaic performances of PSCs. Ultraviolet photoemission spectroscopy (UPS) spectra of the dopant-free PTAA

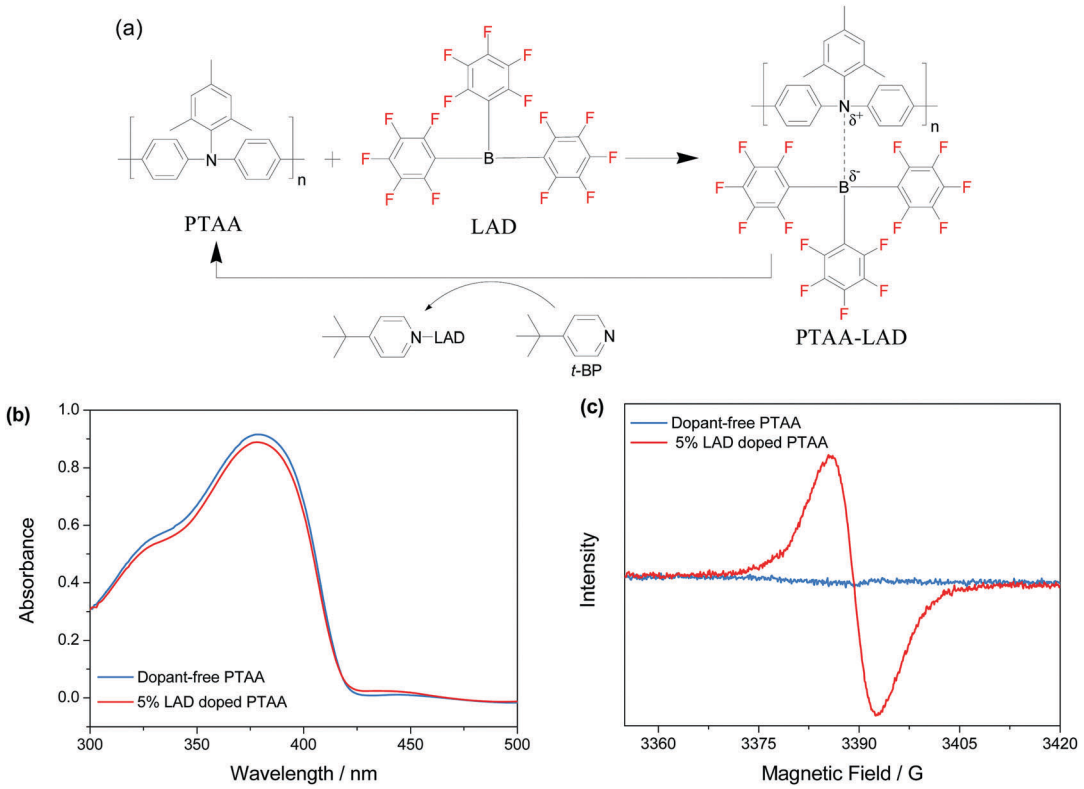

Fig. 1 (a) Molecular structures of PTAA and LAD, and reversible formation of an adduct between Lewis basic PTAA and Lewis acidic LAD in solution. (b) UV-Vis absorption spectra of dopant-free and 5% LAD doped PTAA films. (c) ESR spectra of dopant-free PTAA and 5% LAD doped PTAA.

films and those doped with 5% LAD and Li-TFSI/*t*-BP were recorded. The onset (E_i) and cut-off ($E_{cut\text{-}off}$) energy regions in the UPS spectra are shown in Fig. 2b and c, respectively. Both E_i and $E_{cut\text{-}off}$ are negatively shifted upon doping 5% LAD and Li-TFSI/*t*-BP. According to the equation $\phi = 21.22 - (E_{cut\text{-}off} - E_i)$, the HOMO levels with respect to the vacuum level of dopant-free PTAA, PTAA: 5% LAD and PTAA: Li-TFSI/*t*-BP are −4.91, −5.20 and −5.14 eV, respectively (Fig. S6, ESI†). It is worth noting that the dopant change from Li-TFSI/*t*-BP to LAD shifts the HOMO level downward, which is helpful for collecting the photogenerated holes in the perovskite film with a low energy loss, thus higher open circuit voltage (V_{OC}) is expected for PSCs with 5% LAD doped PTAA as the HTL.[45]

Photovoltaic performances

To examine the capability of LAD to serve as an efficient dopant for PTAA in PSCs, the conventional n–i–p thin-film PSCs with a configuration of FTO (400 nm)/compact TiO_2 (c-TiO_2, 20 nm)/

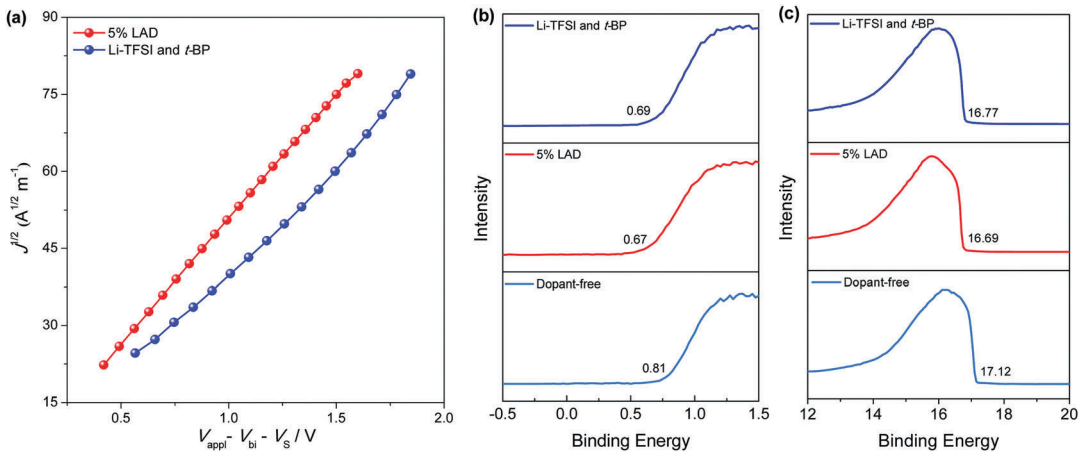

Fig. 2 (a) $J^{1/2}$–V characteristics of the PTAA with different dopants based on hole-only devices: ITO/PEDOT:PSS/PTAA/MoO_3/Al. UPS spectra in the (b) onset and the (c) cut-off energy regions of PTAA films with different dopants.

mesoporous TiO_2 (m-TiO_2, 100 nm)/$CH_3NH_3PbI_3$ (300 nm)/HTL (80 nm)/Au (100 nm) were fabricated and measured. The complete device architecture is illustrated in Fig. 3a, with a representative cross-sectional scanning electron microscopy (SEM) image provided in Fig. 3b, which demonstrates that a dense, compact and uniform perovskite film has been obtained, and clearly distinguishes the PTAA HTL and TiO_2 ETL in the device. The characterization of the perovskite film including surface topography, optical absorption, photoluminescence spectroscopy and XRD is shown in Fig. S7 (ESI†). Fig. 3c shows the *J–V* curves of devices fabricated with different concentrations of LAD for PTAA, and the corresponding photovoltaic parameters are summarized in Table 1. The PSC made of the pristine PTAA without doping (0%) shows a rather low PCE of 12.73% with a short circuit photocurrent density (J_{SC}) of 19.79 mA cm^{-2}, a V_{OC} of 0.99 V and a FF of 0.65. The inferior performance can be ascribed to the low hole mobility of PTAA in its pristine form (Fig. S5, ESI†). Encouragingly, the PSCs show significantly improved performances by doping PTAA with LAD. As the LAD dopant concentration increases, the PCE first increases, reaches a maximum value at 5%, and then decreases (Fig. 3d). Under the best doping concentration of 5% LAD, a champion PCE of 19.01% was obtained, with a J_{SC} of 22.35 mA cm^{-2}, a V_{OC} of 1.05 V and an exceptional FF of 0.81 (Fig. 3e). To the best of our knowledge, such a PCE of 19.01% is the best recorded for PSCs with novel dopants in HTLs reported so far. Meanwhile, we are pleasantly surprised by the fact that the PCE of the PSC based on 5% LAD outperforms the best control device with Li-TFSI and *t*-BP doped PTAA (PCE = 17.77%, J_{SC} = 22.34 mA cm^{-2}, V_{OC} = 1.02 V and FF = 0.78). To ensure the reliability of the *J–V* measurement, the steady-state J_{SC} and PCE of the PSCs were recorded under AM 1.5G illumination with 50 s light on/off cycles, as shown in Fig. 2f and g. All the devices exhibit stable performances and an extremely fast photoresponse. Upon investigating the switching behavior over 600 s, the LAD-based PSC exhibits a PCE of 18.76% with a steady-state J_{SC} of 21.32 mA cm^{-2}, whereas the PSC using Li-TFSI/*t*-BP achieves a steady-state J_{SC} of 20.36 mA cm^{-2} and a steady-state efficiency of 17.51%. These values are very close to the efficiency and J_{SC} obtained from the *J–V* measurements. Meanwhile, to further verify the reproducibility of this improvement, 45 PSCs based on 5% LAD and Li-TFSI/*t*-BP were fabricated and tested under AM 1.5G illumination with reverse scan. Fig. 3h displays a histogram of the PCEs. It is clear that the devices show good reproducibility and the PSCs based on the 5% LAD exhibit a higher average PCE (17.65 ± 1.18%) than those based on the Li-TFSI and *t*-BP (16.39 ± 1.38%). Therefore, this is the first substantial report which experimentally elucidates that on the performance scale, PSCs based on a novel dopant for the HTL can practically outperform devices based on the state-of-the-art bi-dopants Li-TFSI/*t*-BP. In addition, the statistical distributions of J_{SC}, V_{OC} and FF are also in good agreement with our observations from the champion devices (Fig. S8, ESI†). On the basis of these observations, we can conclude that by replacing Li-TFSI and *t*-BP with LAD as a potential dopant for PTAA, the photovoltaic parameters including PCE, V_{OC} and FF have been remarkably improved. These results indicate that LAD is a promising dopant for PTAA to construct highly efficient PSCs. To confirm the accuracy of the J_{SC} measurements in *J–V* curves, we integrated the relevant current densities from the incident photon-to-electron conversion efficiency (IPCE) spectra (Fig. 3i). The integrated J_{SC} values are 21.71 and 21.58 mA cm^{-2} for the cells using the 5% LAD and Li-TFSI/*t*-BP as dopants, respectively, which are in good agreement with J_{SC} from *J–V* measurements.

Interfacial charge extraction performances

In order to analyze and elucidate the excellent photovoltaic performances and the mechanism of charge extraction at the perovskite/HTL interface with ultrafast time resolution in the ps to ns regime, we performed femtosecond transient absorption (fs-TA) spectroscopy for the bilayered $CH_3NH_3PbI_3$/5% LAD doped PTAA and $CH_3NH_3PbI_3$/Li-TFSI and *t*-BP doped PTAA. Fig. 4a and b show the bird's eye graphs of the ΔOD as a function of wavelength and delay time. The typical ΔOD *versus* wavelength plots at various delay times are shown in Fig. S9c and d (ESI†). It can be seen that the femtosecond laser excitation produces a negative ground state bleaching (GSB) band at 670–800 nm, which is related to the fluorescence emission from the perovskite. By probing at the GSB peak, the TA delay kinetics were investigated following double exponential function fitting analyses: $y = y_0 + A_1 \exp\left(-\frac{t}{\tau_1}\right) + A_2 \exp\left(-\frac{t}{\tau_2}\right)$, as shown in Fig. 4c. The faster time constants (τ_1, <1000 ps response) are related to the hole extraction from the photo-excited $CH_3NH_3PbI_3$ to the HTL; the slower time constants (τ_2, >1 ns to 1 μs time scale) can be ascribed to the $CH_3NH_3PbI_3$ excited-state delay time or recombination dynamics of the $CH_3NH_3PbI_3$ absorber.[31] According to fitted results, it was found that the faster delay lifetime (τ_1) reduced from 377 to 309 ps when 5% LAD was employed to replace Li-TFSI/*t*-BP, indicating faster charge extraction in the 5% LAD doped PTAA film. The faster charge extraction was further investigated by using time-resolved photoluminescence (TRPL). As shown in Fig. 4d, the PL lifetime is significantly reduced in perovskite layers covered with 5% LAD and Li-TFSI/*t*-BP doped PTAA layers, indicating effective hole extraction from the $CH_3NH_3PbI_3$ to the HTL in both cases. Further, the average PL delay time reduced from 11.93 ns for the perovskite/Li-TFSI and *t*-BP doped PTAA to 4.83 ns when LAD was used as a novel dopant for PTAA (Table S1, ESI†), which means that the interfacial hole extraction between the 5% LAD doped PTAA layer and perovskite is faster and more efficient than that of the Li-TFSI and *t*-BP doped PTAA/perovskite interface. Thus, the results from TRPL measurements are consistent with fs-TA behaviors. Consequently, the faster and more efficient hole extraction would suppress charge recombination, correspondingly leading to the improved efficiency of PSCs. Therefore, the fs-TA and TRPL results highlight that LAD is a superior dopant for highly efficient PSCs and simultaneously accounts for the enhancement of efficiency when PTAA is doped with 5% LAD.

To further understand the interfacial charge transfer and recombination processes in PSCs, electrical impedance spectroscopy (EIS)

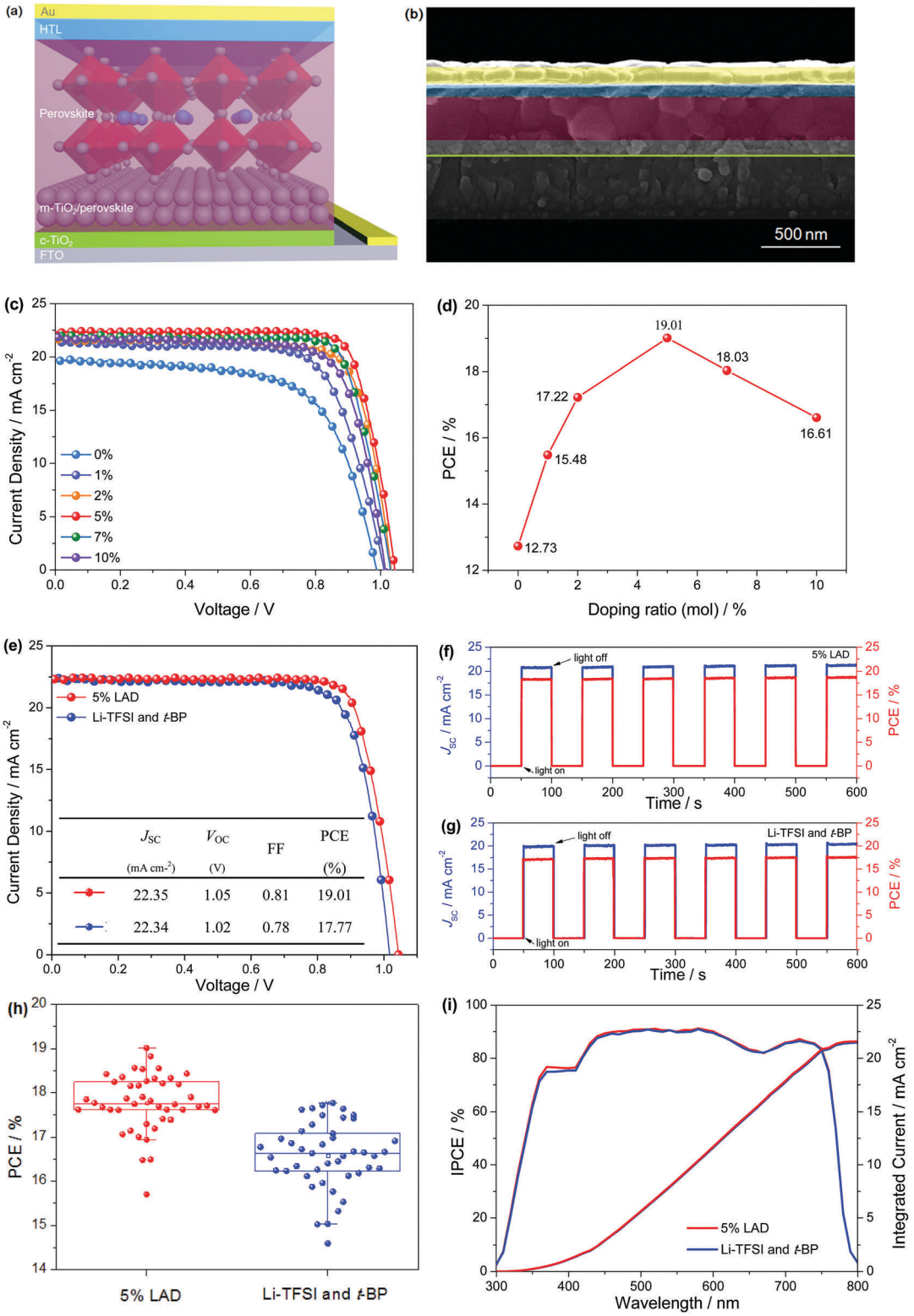

Fig. 3 (a) Schematic configuration of PSCs. (b) Cross-sectional SEM image of a completed PSC. (c) *J*–*V* curves for PSCs employing different doping concentration of LAD in PTAA; the measurements were carried out under 100 mW cm^{-2}, AM 1.5 simulated irradiation with reverse scan (scan rate = 100 mV s^{-1}). (d) The best PCE from the 45 devices for each doping concentration. (e) *J*–*V* curves for the champion devices based on 5% LAD and Li-TFSI/*t*-BP doped PTAA. (f and g) The steady-state photocurrent output at the maximum power point and their corresponding power output with 50 s light on/off cycles of 5% LAD and Li-TFSI/*t*-BP doped PTAA as the HTL, respectively. (h) Statistical distribution of the PCEs for PSCs with 5% LAD and Li-TFSI/*t*-BP doped PTAA as the HTL. (i) IPCE spectra and integrated current densities for the devices based on 5% LAD and Li-TFSI/*t*-BP doped PTAA.

Table 1 Photovoltaic parameters of PSCs based on different dopants for PTAA. Measurements were performed under AM 1.5G illumination (100 mW cm^{-2}) with reverse scan

Dopant	J_{sc}/mA cm^{-2}	V_{oc}/V	FF	PCE/%
Dopant-free	19.79	0.99	0.65	12.73
1% LAD	21.59	1.01	0.71	15.48
2% LAD	21.71	1.03	0.77	17.22
5% LAD	22.35	1.05	0.81	19.01
7% LAD	21.89	1.03	0.80	18.03
10% LAD	21.71	1.02	0.75	16.61
Li-TFSI and *t*-BP	22.34	1.02	0.78	17.77

was measured at a bias of 0.8 V under simulated AM 1.5 illumination.[46] The impedance behavior in the different dopants-based PSCs is shown in Fig. 4e. As shown in Fig. 4e, two distinct regions can be observed in the Nyquist plot: a high frequency regime correlated with the charge recombination process and a low frequency regime correlated with slow dielectric and ionic relaxation in perovskite films.[46] The fitting results (Fig. S10 and Table S2, ESI†) reveal that the PSC based on 5% LAD exhibits a larger recombination resistance (R_{rec} = 78.29 Ω) than that based on Li-TFSI and *t*-BP (R_{rec} = 54.93 Ω). A larger R_{rec} value means a slower charge recombination rate and a smaller dark current, ultimately achieving a higher V_{OC}, which is consistent with the changing

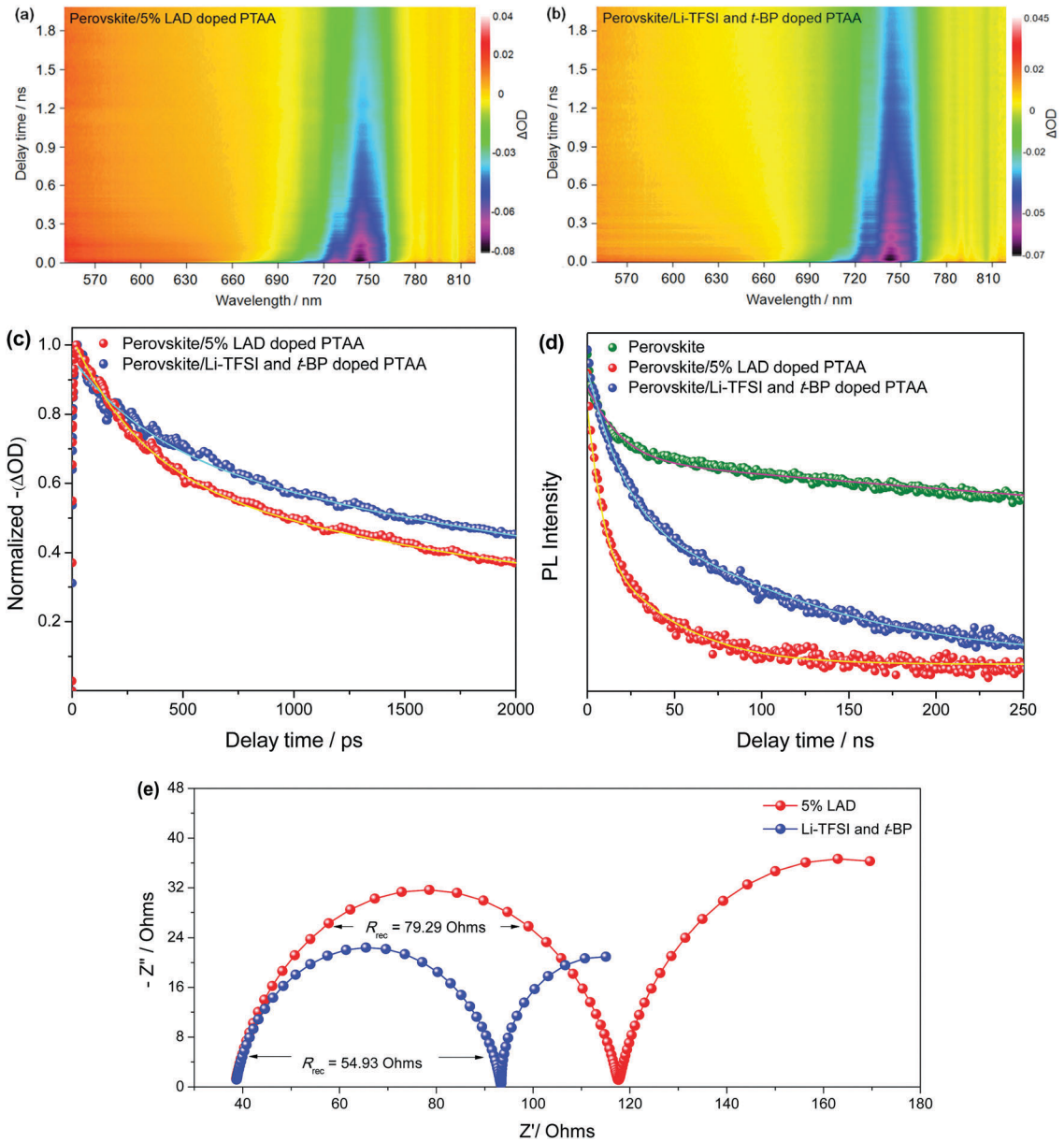

Fig. 4 Bird's eye fs-TA spectra of bilayered (a) perovskite/5% LAD doped PTAA and (b) perovskite/Li-TFSI and *t*-BP doped PTAA films, excited at 365 nm. (c) Normalized bleaching kinetics for perovskite/5% LAD doped PTAA and perovskite/Li-TFSI and *t*-BP doped PTAA probed at 748 nm. (d) TRPL spectra of glass/perovskite, glass/perovskite/5% LAD doped PTAA, glass/perovskite/Li-TFSI and *t*-BP doped PTAA samples. (e) Nyquist plots of PSCs were measured at a bias of 0.8 V under simulated AM 1.5 illumination.

tendencies of *Voc* values obtained in *J–V* curves (Fig. 3e). Therefore, the EIS analysis provides convincing evidence that the 5% LAD doped PTAA can optimize the $CH_3NH_3PbI_3$/PTAA interface and improve hole extraction from $CH_3NH_3PbI_3$ to PTAA, ultimately reducing charge recombination.

Hysteresis

PSCs usually suffer from a hysteresis effect in *J–V* measurements, *i.e.*, a discrepancy of the performance between two voltage sweeping directions and different scan rates, which leads to an inaccurate estimation of the device performance.[28] Therefore, besides investigating the photovoltaic performances, the hysteresis behavior still needs to be studied. The *J–V* characteristics were measured from V_{OC} to J_{SC} (reverse scan) and from J_{SC} to V_{OC} (forward scan) with different scan rates ranging from 10 mV s^{-1} to 100 mV s^{-1} to investigate the hysteresis of PSCs fabricated using different dopants (5% LAD and Li-TFSI/*t*-BP), as shown in Fig. 5a and b. The hysteresis index (HI)

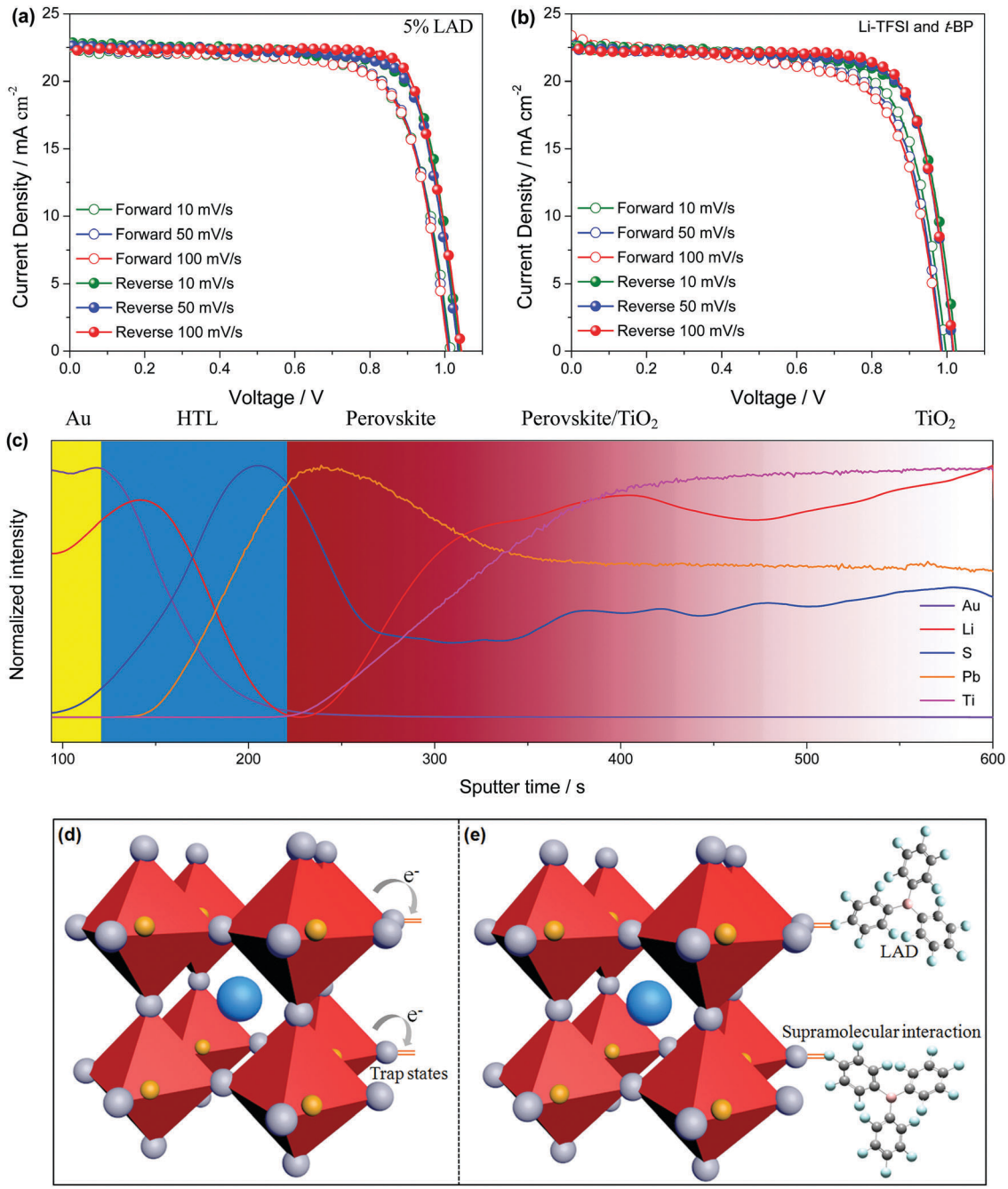

Fig. 5 *J–V* curves of devices based on (a) 5% LAD and (b) Li-TFSI/*t*-BP doped PTAA measured at reverse and forward scans with different scan rates: 10, 50 and 100 mV s^{-1}. (c) Secondary ion mass spectroscopy depth profile of PSCs based on Li-TFSI and *t*-BP doped PTAA as the HTL. (d and e) Schematic of the mechanism for reduced hysteresis by LAD surface passivation.

is used to quantify the degree of hysteresis by the following equation:[44]

$$\mathrm{HI} = \frac{J_{\mathrm{RS}}\ (0.8V_{\mathrm{OC}}) - J_{\mathrm{FS}}\ (0.8V_{\mathrm{OC}})}{J_{\mathrm{RS}}\ (0.8V_{\mathrm{OC}})} \quad (1)$$

where J_{RS} (0.8 V_{OC}) and J_{FS} (0.8 V_{OC}) represent the photocurrent density at 80% of V_{OC} for the reverse scan and forward scan, respectively. A device without hysteresis presents a HI of zero, while a higher value of HI indicates a more pronounced hysteresis. In Table S3 (ESI†), HI values are listed together with photovoltaic parameters depending on the scan direction and scan rate. It is clear from Table S3 (ESI†) that the PSC based on LAD shows smaller HI values than the device based on Li-TFSI and *t*-BP doped PTAA at all scan rates, which means that the LAD based device has relatively low hysteresis. Although the PSC based on LAD is not strictly hysteresis-free, such low hysteresis is extremely similar to the highest reported PSC efficiency by Seok *et al.*[12] Therefore, it is reasonable to believe that LAD is an efficient dopant for PTAA to reduce hysteresis. The origin of LAD-based PSCs with lower hysteresis has been explained on the basis of two mechanisms: (i) extrinsic ion migration. One major consequence of the larger *J–V* hysteresis in PSCs based on Li-TFSI and *t*-BP as dopants is believed to the Li^+-ion migration.[29] By using time-of-flight secondary-ion mass spectrometry (TOF–SIMS), we prove that an extrinsic Li^+ ion, when only added as a dopant (Li-TFSI) in the PTAA layer, can migrate across the perovskite absorber layer and accumulate in the TiO_2 layer. As shown in Fig. 5c, lithium is primarily located in the HTL (which is determined using the element S from the $TFSI^-$ anions of the dopant) and TiO_2 layer, which results from lithium diffusion across the device. Meanwhile, it is interesting to note that lithium concentration does not follow a simple Fickian diffusion distribution; it rises to a higher concentration in the TiO_2 layer than in the perovskite layer. This suggests a higher affinity of Li^+ ions to TiO_2 than to perovskite. The accumulation of Li^+ ions at the TiO_2 would strongly affect PSC operation and hysteresis. Thus, our results open a possible avenue to mitigate the hysteresis issue by developing non-ionic dopants. (ii) Passivation of trap states. The lower hysteresis may also arise from the trap states at the perovskite surface being passivated by LAD. The trap states formed by iodine ions cause recombination of the carriers at the surface (Fig. 5d).[47,48] The strong electron acceptor characteristic of LAD enables it to form a supramolecular interaction with halide ions through halogen bonding (Fig. 5e), which results in the passivation of trap states and reduction of hysteresis.[49] In addition, hysteresis is very sensitive to energy level offsets at the interfaces, so another possible explanation for the reduced hysteresis could be the shift in the HOMO associated with the LAD doping (Fig. S6, ESI†).[50] The *J–V* characteristics of the PSCs based on other LAD doping concentrations have also been investigated under different scan rates and scan directions, and the corresponding *J–V* curves and photovoltaic parameters are shown in Fig. S11 and Table S4 (ESI†).

Stability

Finally, the long-term stability of PSCs based on the dopants LAD and Li-TFSI/*t*-BP without encapsulation was tested for 70 days under air exposure. As shown in the *J–V* curves (Fig. S12, ESI†), the LAD-based PSC still maintains 78% of its initial efficiency after 70 days. By contrast, the PCE of the Li-TFSI/*t*-BP based PSC drastically decays and just retains 0.32% of the original efficiency after the same aging period. The excellent stability of the LAD-based device can be attributed to its lack of deliquescent or hygroscopic dopants and the hydrophobicity of LAD (Fig. S13, ESI†), thereby leading to tightly protected HTL and perovskite layers from air degradation. Conversely, the poor stability of the Li-TFSI/*t*-BP based PSC is mainly ascribed to hygroscopic Li-TFSI and harmful *t*-BP, resulting in perovskite and HTL degradation due to corrosion in the presence of moisture and oxygen through the unstable PTAA layer (Fig. S14 and S15, ESI†).

To *in situ* characterize the phase change of the $CH_3NH_3PbI_3$ degradation process in complete devices with different HTL dopants, synchrotron-based two dimensional grazing incidence X-ray diffraction (2D-GIXRD) techniques have been conducted. Fig. 6a illustrates a schematic of the 2D-GIXRD setup for probing the crystalline information of the perovskite layer. By varying the incident angle, one can change the penetration depth of the X-rays from several nanometers up to tens of micrometers. Fig. 6b and c show the 2D-GIXRD profiles of the fresh and aged PSCs (70 days of air exposure without encapsulation) with Li-TFSI/*t*-BP doped PTAA as the HTL, respectively. It is clear that key features of the perovskite diffraction pattern can be observed at $q \approx 10$, 20 and 23 nm^{-1}, consistent with reflection from the (110), (220) and (310) lattice planes, respectively.[51] As the Li-TFSI/*t*-BP-based PSC was exposed to air for 70 days, an additional diffraction spot appeared at $q \approx 9$ nm^{-1}, which could be assigned to reflection from the (001) plane of PbI_2, suggesting that the perovskite was decomposed. In contrast, no PbI_2 phase was observed in the fresh PSC with Li-TFSI/*t*-BP as dopants and the aged PSC with LAD as dopants (Fig. 6d). The absence of the PbI_2 phase under the same aging conditions of the LAD-based PSC suggests that the novel dopant LAD can effectively improve the perovskite film stability due to the hydrophobic property.

Further, an SEM and an optical microscope were used to *in situ* investigate the top view of the time-lapsed PTAA layers in PSCs. It is found that the LAD doped PTAA layer shows a uniform surface coverage on the perovskite crystals (Fig. S16a, ESI†), and no pinholes appeared even after 70 days of air exposure without encapsulation (Fig. 6e and Fig. S16b, ESI†). However, the Li-TFSI and *t*-BP doped PTAA layer presents a non-uniform surface on the top of the perovskite film with aggregation and crystallization (Fig. S17a, ESI†), which is associated with accumulation of Li salt.[31] Correspondingly, the accumulated Li salt prefers to absorb the moisture in the air, resulting in accelerated degradation of the HTL and formation of pinholes (Fig. 6f and Fig. S17b, ESI†). The pinholes have great influence on the stability of PSCs from two aspects:[52] (1) pinholes facilitate moisture migration through the HTL to reach the perovskite layer, hence triggering further degradation; (2) pinholes facilitate component

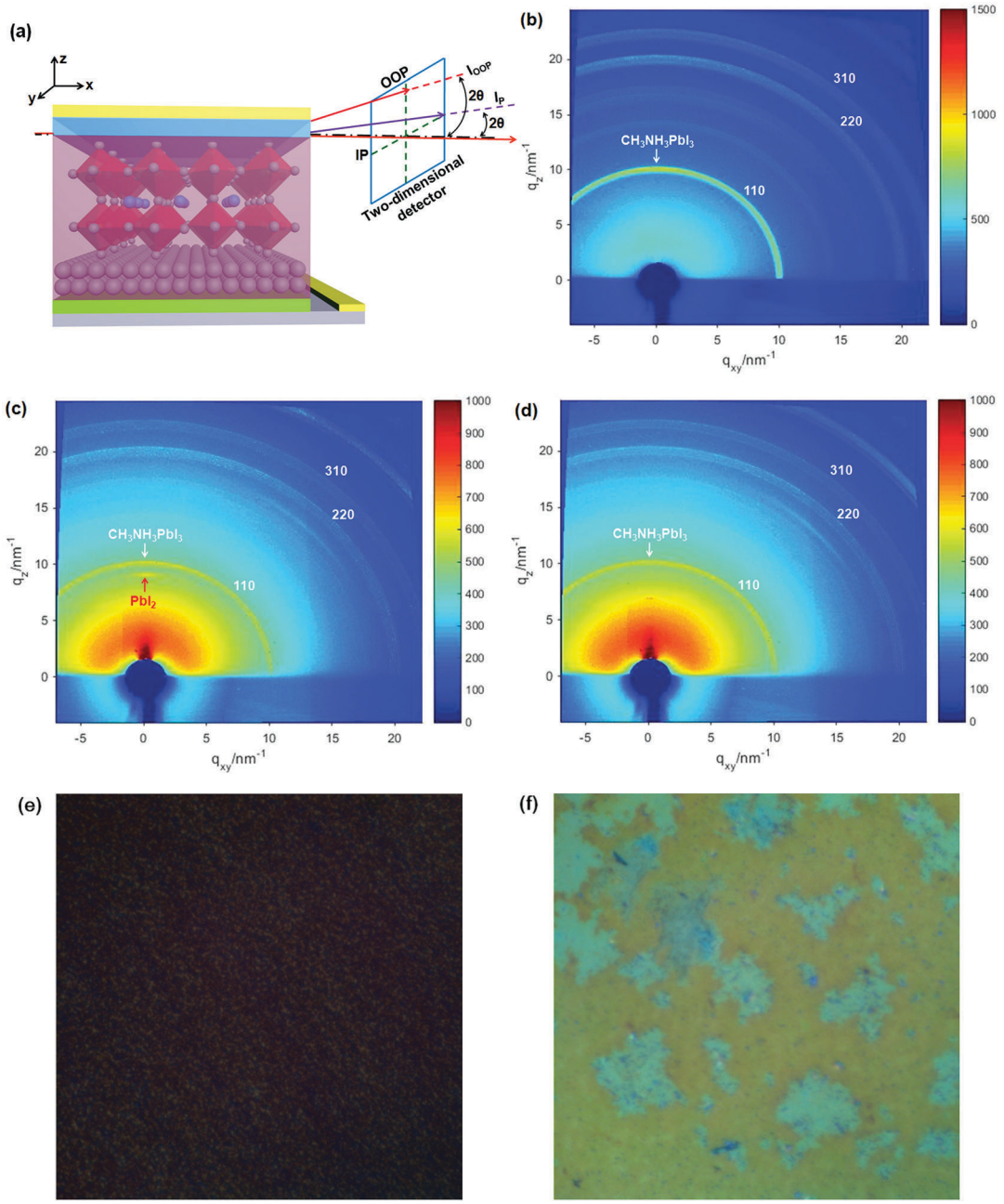

Fig. 6 (a) A schematic of the 2D-GIXRD setup for probing the crystalline information of the perovskite layer, where θ_{IN}, 2θ, I_{IN}, I_{OOP} and I_{IP} are the beam incident angle, the scattering angle, the incoming beam, the scattering beam in the out-of-plane and in-plane directions, respectively. (b) 2D-GIXRD pattern of a fresh PSC with Li-TFSI/*t*-BP doped PTAA. 2D-GIXRD patterns of aged PSCs (70 days under ambient conditions without encapsulation) with (c) Li-TFSI/*t*-BP and (d) 5% LAD as PTAA dopants, respectively. Microscope images of PTAA films in PSCs with (e) 5% LAD and (f) Li-TFSI/*t*-BP as dopants after long-term aging for 70 days under air exposure without encapsulation.

elements from the perovskite (*e.g.*, iodine) to migrate to the top surface and degrade the perovskite. Thus, combining the superior hydrophobicity, absence of any hydrophilic and harmful dopants and the uniform layer of the LAD doped PTAA film, the stability of the LAD-based PSC is far better than that with Li-TFSI and *t*-BP. From these phenomena, high stability of PSCs is expected to be obtained by avoiding deliquescent and hygroscopic additives and developing hydrophobic dopants.

Conclusion

In summary, we have developed a novel dopant LAD for PTAA to achieve high-efficiency, hysteresis-less and stable PSCs. We demonstrated that doped Lewis basic PTAA with the Lewis acidic LAD would form an adduct PTAA-LAD, enhance hole mobility and down-shift the HOMO level, resulting in significantly improved hole extraction as well as reduced charge recombination. With such excellent characteristics, the corresponding PSC

based on 5% LAD doped PTAA achieved an exceptional FF of 0.81 and a PCE of up to 19.01%, the highest PCE reported for PSCs based on novel dopants in the HTL, which was much higher than that of the control device with well-known bi-dopants Li-TFSI/*t*-BP (17.77%) or previously reported p-type dopants. This is the first reported PSC with a novel dopant for the HTL showing better efficiency than that with standard bi-dopants Li-TFSI/*t*-BP to date. Remarkably, the lower *J–V* hysteresis and much better long-term stability of up to 70 days under ambient conditions without encapsulation were observed for the PSC based on LAD doped PTAA. Characterizations suggest that the reduced hysteresis can be ascribed to the non-extrinsic Li^+-ion migration and trap states at the perovskite surface that can be passivated by LAD. The outstanding environmental stability of the LAD based PSC is plausibly attributed to the high hydrophobicity, uniform HTL layer without aggregation and crystallization and the absence of any hydrophilic and harmful dopants.

We unambiguously believe that LAD has tremendous potential to replace Li-TFSI/*t*-BP and this innovative strategy of designing a fluorine-containing hydrophobic Lewis acidic dopant will provide an important future direction for developing high-efficiency, hysteresis-less and stable PSCs.

Conflicts of interest

There are no conflicts to declare.

Acknowledgements

We are grateful to the National Natural Science Foundation of China (Grant no. 21572030, 21402023) and the Technology Innovative Research Team of Sichuan Province of China (No. 2015TD0005) for financial support. We thank Shanghai Synchrotron Radiation Facility (SSRF) BL14B1 for 2D-GIXRD measurements. We also thank Prof. Haoli Zhang, Chunlin Sun and Xiangfeng Shao, who are from State Key Laboratory of Applied Organic Chemistry at Lanzhou University, for providing fs-TA spectra measurements.

References

1 A. Kojima, K. Teshima, Y. Shirai and T. Miyasaka, *J. Am. Chem. Soc.*, 2009, **131**, 6050–6051.
2 S. D. Stranks, G. E. Eperon, G. Grancini, C. Menelaou, M. J. P. Alcocer, T. Leijtens, L. M. Herz, A. Petrozza and H. J. Snaith, *Science*, 2013, **342**, 341–344.
3 Y. Ogomi, A. Morita, S. Tsukamoto, T. Saitho, N. Fujikawa, Q. Shen, T. Toyoda, K. Yoshino, S. S. Pandey, T. Ma and S. Hayase, *J. Phys. Chem. Lett.*, 2014, **5**, 1004–1011.
4 H. Oga, A. Saeki, Y. Ogomi, S. Hayase and S. Seki, *J. Am. Chem. Soc.*, 2014, **136**, 13818–13825.
5 B. Saparov and D. B. Mitzi, *Chem. Rev.*, 2016, **116**, 4558–4596.
6 J. Burschka, A. Dualeh, F. Kessler, E. Baranoff, N. L. Cevey-Ha, C. Yi, M. K. Nazeeruddin and M. Grätzel, *J. Am. Chem. Soc.*, 2011, **133**, 18042–18045.
7 H. S. Kim, C. R. Lee, J. H. Im, K. B. Lee, T. Moehl, A. Marchioro, S. J. Moon, R. Humphry-Baker, J. H. Yum, J. E. Moser, M. Grätzel and N. G. Park, *Sci. Rep.*, 2012, **2**, 591.
8 J. Burschka, N. Pellet, S. J. Moon, R. Humphry-Baker, P. Gao, M. K. Nazeeruddin and M. Grätzel, *Nature*, 2013, **499**, 316–319.
9 M. Liu, M. B. Johnston and H. J. Snaith, *Nature*, 2013, **501**, 395–398.
10 N. J. Jeon, J. H. Noh, Y. C. Kim, W. S. Yang, S. Ryu and S. I. Seok, *Nat. Mater.*, 2014, **13**, 897–903.
11 H. Zhou, Q. Chen, G. Li, S. Luo, T. B. Song, H. S. Duan, Z. Hong, J. You, Y. Liu and Y. Yang, *Science*, 2014, **345**, 542–546.
12 W. S. Yang, B.-W. Park, E. H. Jung, N. J. Jeon, Y. C. Kim, D. U. Lee, S. S. Shin, J. Seo, E. K. Kim, J. H. Noh and S. I. Seok, *Science*, 2017, **356**, 1376–1379.
13 National Renewable Energy Laboratory, Best Research Cell Efficiency, http://www.nrel.gov/ncpv/images/efficiency_chart.jpg.
14 W. E. I. Sha, X. Ren, L. Chen and W. C. H. Choy, *Appl. Phys. Lett.*, 2015, **106**, 221104.
15 H. Tan, A. Jain, O. Voznyy, X. Lan, F. P. G. D. Arquer, J. Z. Fan, R. Quintero-Bermudez, M. Yuan, B. Zhang, Y. Zhao, F. Fan, P. Li, L. N. Quan, Y. Zhao, Z.-H. Lu, Z. Yang, S. Hoogland and E. H. Sargent, *Science*, 2017, **355**, 722–726.
16 T. Bu, X. Liu, Y. Zhou, J. Yi, X. Huang, L. Luo, J. Xiao, Z. Ku, Y. Peng, F. Huang, Y.-B. Cheng and J. Zhong, *Energy Environ. Sci.*, 2017, **10**, 2509–2515.
17 M. M. Byranvand, T. Kim, S. Song, G. Kang, S. U. Ryu and T. Park, *Adv. Energy Mater.*, 2017, **7**, 1702235.
18 F. Giordano, A. Abate, J. P. Correa Baena, M. Saliba, T. Matsui, S. H. Im, S. M. Zakeeruddin, M. K. Nazeeruddin, A. Hagfeldt and M. Grätzel, *Nat. Commun.*, 2016, **7**, 10379.
19 L. Hu, T. Liu, J. Duan, X. Ma, C. Ge, Y. Jiang, F. Qin, S. Xiong, F. Jiang, B. Hu, X. Gao, Y. Yi and Y. Zhou, *Adv. Funct. Mater.*, 2017, **27**, 1703254.
20 J. Peng, Y. Wu, W. Ye, D. A. Jacobs, H. Shen, X. Fu, Y. Wan, T. Duong, N. Wu, C. Barugkin, H. T. Nguyen, D. Zhong, J. Li, T. Lu, Y. Liu, M. N. Lockrey, K. J. Weber, K. R. Catchpole and T. P. White, *Energy Environ. Sci.*, 2017, **10**, 1792–1800.
21 J. Peng, T. Duong, X. Zhou, H. Shen, Y. Wu, H. K. Mulmudi, Y. Wan, D. Zhong, J. Li, T. Tsuzuki, K. J. Weber, K. R. Catchpole and T. P. White, *Adv. Energy Mater.*, 2017, **7**, 1601768.
22 J. Pan, C. Mu, Q. Li, W. Li, D. Ma and D. Xu, *Adv. Mater.*, 2016, **28**, 8309–8314.
23 W. Ke, C. Xiao, C. Wang, B. Saparov, H. S. Duan, D. Zhao, Z. Xiao, P. Schulz, S. P. Harvey, W. Liao, W. Meng, Y. Yu, A. J. Cimaroli, C. S. Jiang, K. Zhu, M. Al-Jassim, G. Fang, D. B. Mitzi and Y. Yan, *Adv. Mater.*, 2016, **28**, 5214–5221.
24 J. Jiang, Q. Wang, Z. Jin, X. Zhang, J. Lei, H. Bin, Z.-G. Zhang, Y. Li and S. F. Liu, *Adv. Energy Mater.*, 2017, **7**, 1701757.
25 C. Fei, B. Li, R. Zhang, H. Fu, J. Tian and G. Cao, *Adv. Energy Mater.*, 2017, **7**, 1602017.
26 Q. Han, Y. Bai, J. Liu, K.-z. Du, T. Li, D. Ji, Y. Zhou, C. Cao, D. Shin, J. Ding, A. D. Franklin, J. T. Glass, J. Hu,

M. J. Therien, J. Liu and D. B. Mitzi, *Energy Environ. Sci.*, 2017, **10**, 2365–2371.
27 Y. Zhang, Z. Fei, P. Gao, Y. Lee, F. F. Tirani, R. Scopelliti, Y. Feng, P. J. Dyson and M. K. Nazeeruddin, *Adv. Mater.*, 2017, **29**, 1702157.
28 J. Xu, A. Buin, A. H. Ip, W. Li, O. Voznyy, R. Comin, M. Yuan, S. Jeon, Z. Ning, J. J. McDowell, P. Kanjanaboos, J. P. Sun, X. Lan, L. N. Quan, D. H. Kim, I. G. Hill, P. Maksymovych and E. H. Sargent, *Nat. Commun.*, 2015, **6**, 7081.
29 Z. Li, C. Xiao, Y. Yang, S. P. Harvey, D. H. Kim, J. A. Christians, M. Yang, P. Schulz, S. U. Nanayakkara, C.-S. Jiang, J. M. Luther, J. J. Berry, M. C. Beard, M. M. Al-Jassim and K. Zhu, *Energy Environ. Sci.*, 2017, **10**, 1234–1242.
30 J. Luo, C. Jia, Z. Wan, F. Han, B. Zhao and R. Wang, *J. Power Sources*, 2017, **342**, 886–895.
31 W. Tress, *Adv. Energy Mater.*, 2017, **7**, 1602358.
32 K. Aitola, K. Sveinbjörnsson, J.-P. Correa-Baena, A. Kaskela, A. Abate, Y. Tian, E. M. J. Johansson, M. Grätzel, E. I. Kauppinen, A. Hagfeldt and G. Boschloo, *Energy Environ. Sci.*, 2016, **9**, 461–466.
33 N. Arora, M. I. Dar, A. Hinderhofer, N. Pellet, F. Schreiber, S. M. Zakeeruddin and M. Grätzel, *Science*, 2017, **355**, 768–771.
34 C. Chen, W. Zhang, J. Cong, M. Cheng, B. Zhang, H. Chen, P. Liu, R. Li, M. Safdari, L. Kloo and L. Sun, *ACS Energy Lett.*, 2017, **2**, 497–503.
35 Z. Li, J. Tinkham, P. Schulz, M. Yang, D. H. Kim, J. Berry, A. Sellinger and K. Zhu, *Adv. Energy Mater.*, 2017, **7**, 1601451.
36 J. Xu, O. Voznyy, R. Comin, X. Gong, G. Walters, M. Liu, P. Kanjanaboos, X. Lan and E. H. Sargent, *Adv. Mater.*, 2016, **28**, 2807–2815.
37 A. Pellaroque, N. K. Noel, S. N. Habisreutinger, Y. Zhang, S. Barlow, S. R. Marder and H. J. Snaith, *ACS Energy Lett.*, 2017, **2**, 2044–2050.
38 I. Lee, J. H. Yun, H. J. Son and T. S. Kim, *ACS Appl. Mater. Interfaces*, 2017, **9**, 7029–7035.
39 B. Xu, Z. Zhu, J. Zhang, H. Liu, C.-C. Chueh, X. Li and A. K. Y. Jen, *Adv. Energy Mater.*, 2017, **7**, 1700683.
40 W. Li, H. Dong, L. Wang, N. Li, X. Guo, J. Li and Y. Qiu, *J. Mater. Chem. A*, 2014, **2**, 13587–13592.
41 H. Greijer, J. Lindgren and A. Hagfeldt, *J. Phys. Chem. B*, 2001, **105**, 6314–6320.
42 P. Zalar, M. Kuik, Z. B. Henson, C. Woellner, Y. Zhang, A. Sharenko, G. C. Bazan and T. Q. Nguyen, *Adv. Mater.*, 2014, **26**, 724–727.
43 M. J. Frisch, G. W. Trucks, H. B. Schlegel, G. E. Scuseria, M. A. Robb, J. R. Cheeseman, J. A. Montgomery Jr., T. Vreven, K. N. Kudin, J. C. Burant, J. M. Millam, S. S. Iyengar, J. Tomasi, V. Barone, B. Mennucci, M. Cossi, G. Scalmani, N. Rega, G. A. Petersson, H. Nakatsuji, M. Hada, M. Ehara, K. Toyota, R. Fukuda, J. Hasegawa, M. Ishida, T. Nakajima, Y. Honda, O. Kitao, H. Nakai, M. Klene, X. Li, J. E. Knox, H. P. Hratchian, J. B. Cross, V. Bakken, C. Adamo, J. Jaramillo, R. Gomperts, R. E. Stratmann, O. Yazyev, A. J. Austin, R. Cammi, C. Pomelli, J. W. Ochterski, P. Y. Ayala, K. Morokuma, G. A. Voth, P. Salvador, J. J. Dannenberg, V. G. Zakrzewski, S. Dapprich, A. D. Daniels, M. C. Strain, O. Farkas, D. K. Malick, A. D. Rabuck, K. Raghavachari, J. B. Foresman, J. V. Ortiz, Q. Cui, A. G. Baboul, S. Clifford, J. Cioslowski, B. B. Stefanov, G. Liu, A. Liashenko, P. Piskorz, I. Komaromi, R. L. Martin, D. J. Fox, T. Keith, M. A. Al-Laham, C. Y. Peng, A. Nanayakkara, M. Challacombe, P. M. W. Gill, B. Johnson, W. Chen, M. W. Wong, C. Gonzalez and J. A. Pople, *Gaussian 09, Revision A.02*, Gaussian, Inc., Wallingford, CT, 2009.
44 H. S. Kim and N. G. Park, *J. Phys. Chem. Lett.*, 2014, **5**, 2927–2934.
45 J. Luo, F. Han, Z. Wan, H. A. Malik, B. Zhao, L. Chen, C. Jia, X. Zhu, R. Wang and X. Yao, *Electrochim. Acta*, 2017, **257**, 380–387.
46 F. Wang, W. Geng, Y. Zhou, H. H. Fang, C. J. Tong, M. A. Loi, L. M. Liu and N. Zhao, *Adv. Mater.*, 2016, **28**, 9986–9992.
47 A. Abate, M. Saliba, D. J. Hollman, S. D. Stranks, K. Wojciechowski, R. Avolio, G. Grancini, A. Petrozza and H. J. Snaith, *Nano Lett.*, 2014, **14**, 3247–3254.
48 J. Xu, A. Buin, A. H. Ip, W. Li, O. Voznyy, R. Comin, M. Yuan, S. Jeon, Z. Ning and J. J. McDowell, *Nat. Commun.*, 2015, **6**, 1401692.
49 D. Song, D. Wei, P. Cui, M. Li, Z. Duan, T. Wang, J. Ji, Y. Li, J. M. Mbengue, Y. Li, Y. He, M. Trevor and N.-G. Park, *J. Mater. Chem. A*, 2016, **4**, 6091–6097.
50 H. Shen, D. A. Jacobs, Y. Wu, T. Duong, J. Peng, X. Wen, X. Fu, S. K. Karuturi, T. P. White, K. Weber and K. R. Catchpole, *J. Phys. Chem. Lett.*, 2017, **8**, 2672–2680.
51 J. Yang, B. D. Siempelkamp, D. Liu and T. L. Kelly, *ACS Nano*, 2015, **9**, 1955–1963.
52 Z. Hawash, L. K. Ono, S. R. Raga, M. V. Lee and Y. Qi, *Chem. Mater.*, 2015, **27**, 562–569.